Materials Science & Engineering A 944 (2025) 148941

Contents lists available at ScienceDirect

Materials Science & Engineering A

journal homepage: www.elsevier.com/locate/msea

Effect of alloying elements on the mechanical behavior of extruded Mg-Al-Bi alloys

A. Goldman [a], Z.G. Xu [b], B. Li [a,*], Y.L. Liao [a], A. Jordan [a]

[a] Department of Industrial and Manufacturing Systems Engineering, Iowa State University, Ames, IA, 50011, USA
[b] Department of Mechanical Engineering, North Carolina Agricultural and Technical State University, Greensboro, NC, 27411, USA

ARTICLE INFO

Keywords:
Magnesium
Alloying
Deformation
Twinning

ABSTRACT

Rare-earth free magnesium (Mg) alloys are attractive for engineering applications. In this study, we design, cast and extrude six Mg-Al-Bi alloys with the Al% of 3~9 wt% and Bi% of 1~2 wt%. The deformation behaviors of the extruded alloys are examined in uniaxial tension and compression. The microstructure, texture and precipitates are characterized by electron backscatter diffraction (EBSD) and X-ray diffraction (XRD). The results show that, in tension, as the Al% and Bi% increase, the yield stress and ultimate tensile stress consistently increase, but the ductility is mostly retained across the whole range of compositions. Alloying with Bi improves the tensile strength more effectively when the Al% is at the lower range. In compression, Bi only has a moderate effect on strength. The compressive stress-strain curves present a typical sigmoidal shape but the range of low stress deformation, which is dominated by $\{10\bar{1}2\}$ twinning, consistently narrows as the Al% and Bi% increase. This indicates that alloying with Al, especially at high Al%, can effectively suppress $\{10\bar{1}2\}$ twinning. Characterization of the precipitates shows that addition of Bi suppresses the formation of $Mg_{17}Al_{12}$ which is a common, plate-like intermetallic phase parallel to the basal plane in Mg-Al-Zn alloys.

1. Introduction

The deformation behavior and mechanical properties of lightweight magnesium (Mg) alloys have been studied extensively over the past two decades. These materials have the potential to reduce the weight of vehicles and thus improve fuel efficiency. However, their widespread application has not been realized because of their limited room temperature formability which is related to their ductility. Also, Mg alloys are much more difficult to achieve age-hardening through heat treatment than aluminum (Al) alloys [1–3]. Wrought Mg alloys such as rolled or extruded typically present improved strength and ductility than as-cast Mg alloys because of the refined microstructure and more homogeneous chemical composition; however, wrought Mg alloys have a high propensity to develop strong basal texture [4–6], leading to anisotropic deformation behavior that is undesirable. The anisotropic mechanical properties of wrought Mg alloys are a direct result of different deformation modes that are activated when a sample is loaded in tension and compression [6–10].

Much effort has been made to mitigate the anisotropy in the deformation behavior of wrought Mg alloys. One of the effective approaches is to weaken or randomize the basal texture, such that non-basal dislocation slip can be promoted [11–14]. In wrought Mg alloys, the basal planes of individual grains are mostly aligned with the extrusion direction or the rolling direction, so the activities of the non-basal slip (prismatic and pyramidal slip) systems are limited, making it hard to satisfy the von Mises criterion [15] that requires at least five independent slip systems to provide the needed strain compatibility at grain boundaries. This gives rise to the limited room temperature ductility. To weaken the basal texture, severe plastic deformation (SPD) approaches have been used to refine the grain size down to the micron or submicron scale [10,16–20]. The orientations of ultrafine grains are more randomly distributed than that in coarse-grained materials. The refined grain structure offers improved strength and ductility [17,18,21]. Another approach to weaken the basal texture is to design new Mg alloys with rare-earth (RE) elements. Addition of RE to Mg alloys results in the so-called "rare-earth texture" in which the typically strong rod texture in wrought Mg alloys is split, leading to improved ductility. It has been shown that some RE elements effectively weaken the basal texture [6,22,23]. The major drawback of the RE-containing Mg alloys is the high cost of these elements that hinders these alloys from widespread

* Corresponding author.
E-mail address: binl@iastate.edu (B. Li).

https://doi.org/10.1016/j.msea.2025.148941
Received 10 January 2025; Received in revised form 29 July 2025; Accepted 8 August 2025
Available online 10 August 2025

applications.

There have been efforts to study how other alloying elements than RE influence strength and ductility of Mg alloys. Recently, Bi has emerged as a promising alloying element. Several research groups have shown that Bi-containing Mg alloys present good strength and ductility. The Mg-Bi intermetallic Mg_3Bi_2 has a melting point of 823 °C and is more stable than $Mg_{17}Al_{12}$ [24]. The atomic radius of Bi (1.43 Å) is very close to Mg's. The solubility limit of Bi in Mg is up to 9 % [24]. This provides opportunities for thermomechanical processing routes for Bi-containing Mg alloys. Go et al. [25] was able to improve the extrudability of Mg-3Al alloys by adding 5 % Bi. A die exit speed of 67 m/min was achieved, more than 10 times faster than commercial Mg alloys. Meng et al. [26] reported a remarkable room temperature elongation of 43 % in a Mg-1.32Bi-0.74Ca alloy processed by extrusion. The fully recrystallized microstructure showed a weakened $[2\bar{1}\bar{1}2] \parallel$ ED (extrusion direction) texture. A small amount of Bi (0.5–3.0 %) refined the structure of $Mg_{17}Al_{12}$ precipitates which became more continuous in the cast and heat treated AZ91 [27]. However, the tensile ductility steadily decreased with increasing Bi%, but little change was observed in terms of tensile strength. In these works, how Bi affects the deformation behavior of extruded Mg alloys has not been systematically studied.

The purpose of this work is to investigate the effects of alloying elements on the deformation behavior of extruded Mg-Al-Bi alloys. This alloy system is designed to only use inexpensive alloying elements. Al is the most common alloying element for commercial Mg alloys such as AZ series. Al improves the corrosion resistance and the castability of Mg alloys. Six alloy compositions are designed, cast and extruded. Uniaxial tension and compression properties are tested. Effects of Al and Bi on the twinning behavior are analyzed and discussed. Our results offer new insight into the design of Mg alloys without RE.

2. Experimental method

In the present work, six Mg-Al-Bi alloy compositions were designed, cast and thermomechanically processed. The Al concentration was prepared as 3.0 wt%, 6.0 wt%, and 9.0 wt%. Bi was added in concentrations of 1.0 wt% and 2.0 wt%, respectively, to the Mg-Al alloys. These Al concentrations were chosen to correlate with the commercial AZ31, AZ61 and AZ91 alloys. For convenience, our alloys were named following the convention of ABXY, where the Al% and Bi% are in the place of X and Y, respectively. For example, AB31 corresponds to Mg-3.0Al-1.0Bi. Thus, a full list of our alloys were named AB31, AB32, AB62, AB62, AB91, and AB92 with increasing Al and Bi concentration.

The alloys were prepared by melting and casting high purity Mg (99.97 %, US Magnesium), Al (99.999 %, Alfa Caesar) and Bi (99.99 %). Each alloy was melted at 730 °C and then cast into a cylindrical steel mold 40 mm in diameter that was preheated to 300 °C. The casting was conducted in a vacuum filled with argon gas. More details of casting procedure can be found in the work by Xu et al. [28]. The cast ingots were then homogenized, first by heating to 320 °C for 5 h then to 420 °C for 20 h, followed by water quenching. Subsequently, the materials were indirectly extruded at 425 °C, with an extrusion ratio of 30 and a ram speed of 0.2 mm/s. All alloys, including both AB91 and AB92, experienced no cracking during extrusion.

The extruded samples were prepared for characterization by steps of grinding and polishing. First, mechanical grinding was conducted with silicon carbide sandpaper of grit number starting at 400, then to 800 and 1200. Following mechanical grinding, the samples were polished successively on cloths containing 3, 1, and 0.5 μm diamond suspension. The final preparation was completed by electropolishing. A Struers electropolisher (Lectropol 5) was used with an electrolyte (200 proof ethanol + 5 vol% nitric acid + 0.5 vol% perchloric acid). Electropolishing was carried out at room temperature using 20 V for 12 s. Following electropolishing, the samples were quickly rinsed in ethanol and dried with compressed air. The polished samples were then analyzed by electron backscatter diffraction (EBSD) using an FEI Teneo field emission scanning electron microscope (SEM) equipped with an Oxford EBSD detector. The step size for EBSD scanning was 0.5 μm. The operation conditions were 13 nA and 20 kV. For high Al% samples that contain a high volume of precipitates, after electropolishing, the surfaces of these samples were gently wiped with a lint free cloth, which broke and removed the protruding precipitates that otherwise would have interfered with the electron beam during EBSD scanning. The EBSD data was exported to and processed in ATEX [29] for further analyses.

To characterize the precipitates within the Mg-Al-Bi samples, X-ray diffraction (XRD) was performed on a Siemens D500 diffractometer in Bragg-Brentano geometry using a copper X-ray tube operating at 45 kV and 30 mA. The un-extruded AB92 sample was used for scanning from 5° to 70° with a step size of 0.05° and a dwell time of 5 s per step using medium-resolution slits. The XRD data was then analyzed using Jade software version 9.5 (Materials Data Incorporated, Livermore, CA). The Inorganic Crystal Structure Database (ICSD) and the International Centre for Diffraction Data (ICCD) were used to identify the crystalline phases.

Uniaxial tension and compression tests were conducted on the as-extruded Mg-Al-Bi samples. An Instron 3367 machine with a 30 kN load cell was used for mechanical tests. The loading direction was parallel to the extrusion direction. Cylindrical samples were machined for compression, whereas round, dog-bone samples were fabricated for tension. A strain rate of 3.0×10^{-3}/sec was chosen for all the mechanical tests, which was close to the typical range (10^{-4}–10^{-3}/sec) for laboratory testing under quasistatic conditions. Interrupted compression tests were also conducted in which the compression was terminated at strain levels of 2.0 % or 4.0 % of engineering strain, in order to characterize the twinning behavior at the early stage of deformation. For the tensile samples, cylindrical dog-bones with threaded ends were machined and then tested.

3. Results

The grain structure of the as-extruded samples is shown in Fig. 1, which is the inverse pole figure (IPF) maps of the as-extruded samples from the EBSD data. It can be seen that the microstructures of all six samples are composed of equiaxed grains. We also examined the grain morphology on a sample surface parallel to the extrusion direction and found no elongated grains. This indicates that during extrusion, the materials are fully dynamically recrystallized (DRX), which can be attributed to the relatively high extrusion temperature and the large reduction rate. Also, if DRX were incomplete, a bi-modal mixture of large and small grains would be seen. After DRX, a majority of grains are oriented such that their $[11\bar{2}0]$ or $[10\bar{1}0]$ pole is parallel to the extrusion direction, which is typical of the DRXed microstructure of AZ Mg alloys. The (0001) pole figures of all six extruded samples are shown in Fig. 2. All the samples present a strong basal texture which is very similar to that of wrought AZ Mg alloys. This indicates that the addition of Bi to the Mg-Al alloys has little effect on the texture development during extrusion. The basal texture (Fig. 2) is also similar to that in the Mg-3Al-5Bi alloys reported by Go et al. [25].

Fig. 3 shows the grain size distribution of the six extruded Mg-Al-Bi alloys. The overall trend is that, as the Al% and Bi% increase, the average grain size decreases. Thus, the alloy composition has a moderate effect on the grain size of our extruded alloys. This can be understood from the fact that, as the Al% and Bi% increase, the weight fraction of intermetallic phases (as shown below, the precipitates are mainly $Mg_{17}Al_{12}$ and Mg_3Bi_2) increases. The precipitates may stimulate the nucleation of new grains during the early stage of dynamic recrystallization, as reported by a number of researchers [30–32]. The precipitates may also act as a barrier to grain growth and slow down the coarsening rate by pinning down grain boundaries from migrating [24,25,33].

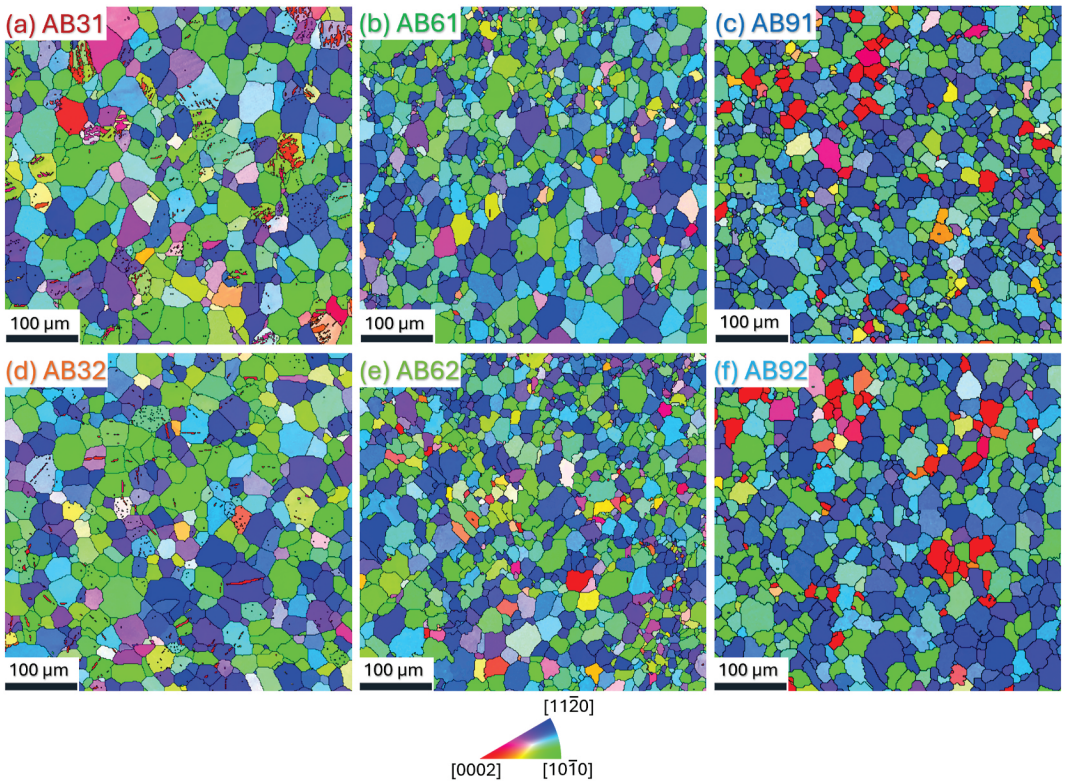

Fig. 1. EBSD Inverse pole figures maps of the as extruded Mg-Al-Bi alloys. The scans are performed on the cross-section perpendicular to the extrusion direction. It can be seen that the microstructure of all the samples is fully recrystallized after extrusion. The alloy composition has a moderate effect on the grain size.

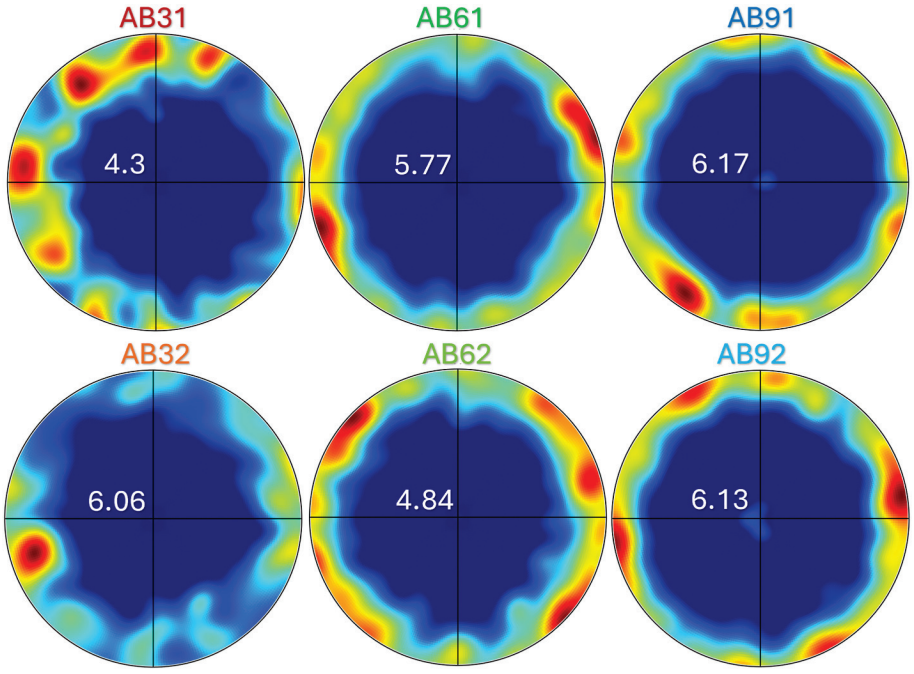

Fig. 2. (0001) basal pole figures of the as extruded Mg-Al-Bi samples obtained from EBSD. The white text shows the maximum intensity for each composition. All pole figures present a strong basal texture, which is typical of wrought Mg alloys.

The XRD results are shown in Fig. 4. Three phases are present in the AB92 alloy, and similar results can be expected in the other alloy compositions. It can be seen that, in addition to the high intensity from the α-Mg which is a Mg-Al solid solution, two additional phases are present. According to the Mg-Bi phase diagram [34], the solubility of Bi in Mg at room temperature is negligible. Thus, it is expected that most of Bi should exist in the form of intermetallics. Fig. 4 shows that the Mg-Bi intermetallics is identified as Mg_3Bi_2, which is consistent with the reports by Guo et al. [35] and Go et al. [25]. Another intermetallic phase is identified as $Mg_{17}Al_{12}$, which is the common β phase in AZ alloys. To

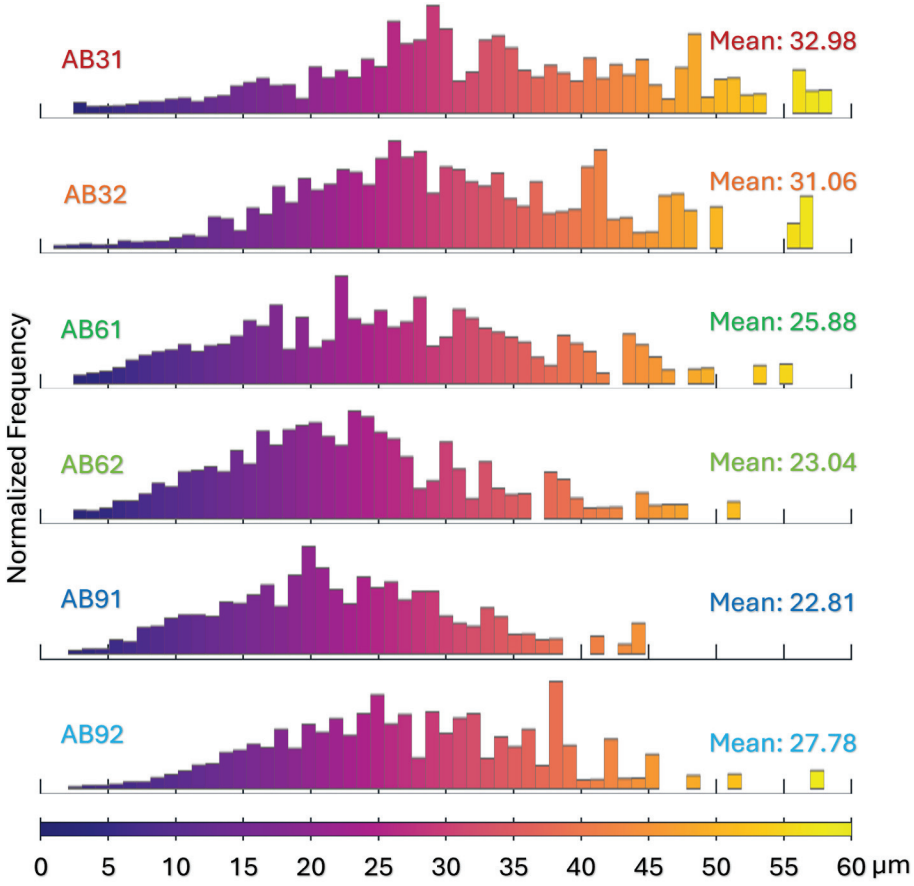

Fig. 3. Grain size distribution of the six as extruded Mg-Al-Bi alloys. The grain size is measured from a 500 by 500 μm area of each sample. In general, the average grain size slightly decreases with increasing alloy concentration.

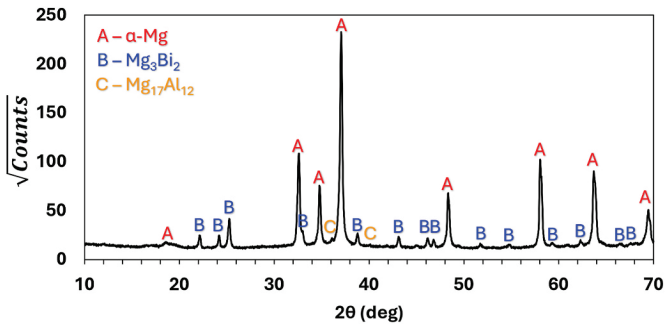

Fig. 4. XRD results of the as-cast AB92 alloy, with α-Mg showing most prominently, followed by Mg_3Bi_2 with distinct peaks, and subtle peaks were detected for $Mg_{17}Al_{12}$ despite the relatively high concentration of Al.

better understand how the size and distribution of the intermetallic phases respond as the alloy concentrations change, a SEM analysis of the microstructure is presented in Figs. 5 and 6.

The secondary electron SEM images in Fig. 5 contain representative areas of the as-extruded samples whose polished surfaces are parallel to the ED. Again, we can see that the grains are equiaxed, indicative of complete DRX. At the lowest concentration of Al and Bi added (AB31), fine (hundreds of nanometers) Mg_3Bi_2 precipitates are dispersed in the matrix. These fine precipitates are also present along most of the grain boundaries (Fig. 5a). In AB32 with the Bi% doubled (Fig. 5b), almost all the grain boundaries are entirely decorated with fine precipitates. Doubling the Bi% results in a larger volume fraction of precipitates. After extrusion, some of these precipitates are dispersed along the ED, forming streaks non-uniformly. In AB31 and AB32, the dominant plate-like $Mg_{17}Al_{12}$ precipitates along the basal plane that are commonly observed in Mg-Al-Zn alloys [36] are not observed in our SEM observations. The lack of plate-like $Mg_{17}Al_{12}$ in the matrix might be because their formation is suppressed by the addition of Bi. To verify this, TEM will be conducted to identify and differentiate these precipitates, and the results will be reported in future work. Fig. 5c shows the size and morphology of the precipitates in AB61 that contains 6 % Al. The higher Al% leads to a substantial increase in the volume fraction of precipitates. The size of the precipitates appears to be coarser than that in AB31 and AB32. More streaking of precipitates can be observed than in AB32. It can also be seen that fewer precipitates are present along the grain boundaries. A similar behavior can be observed in AB62 (Fig. 5d). When the Al% is further increased to 9 % (AB91 in Fig. 5e), coarse precipitates can be seen along with small Mg_3Bi_2 precipitates. EDS analysis indicates that the coarse flake-like precipitates are $Mg_{17}Al_{12}$ (see images at a higher magnification below). In AB92 (Fig. 5f), a similar morphology and distribution of the precipitates can be seen.

At a higher magnification, Fig. 6a–f presents more detailed views of the secondary phases in the extruded alloys. These back scattered electron (BSE) images offer a better phase contrast than secondary electron images in Fig. 5a–f. In Fig. 6a, the Z contrast of BSE highlights the sub-micron Mg_3Bi_2 precipitates (bright dots) at the grain boundaries and throughout the matrix of AB31. In AB32 more Mg_3Bi_2 intermetallics can be seen in the matrix, as well as along the grain boundaries. Fig. 6c shows that in AB61, fewer Mg_3Bi_2 precipitates are present at the grain boundaries while more streaks containing coarser precipitates are present across the grains (Fig. 5c). Fig. 6d shows that, inside the streaks, flake-like $Mg_{17}Al_{12}$ (middle gray) are present and decorated with fine Mg_3Bi_2 precipitates. As the Al% is increased to 9 % (AB91 in Fig. 6e), the

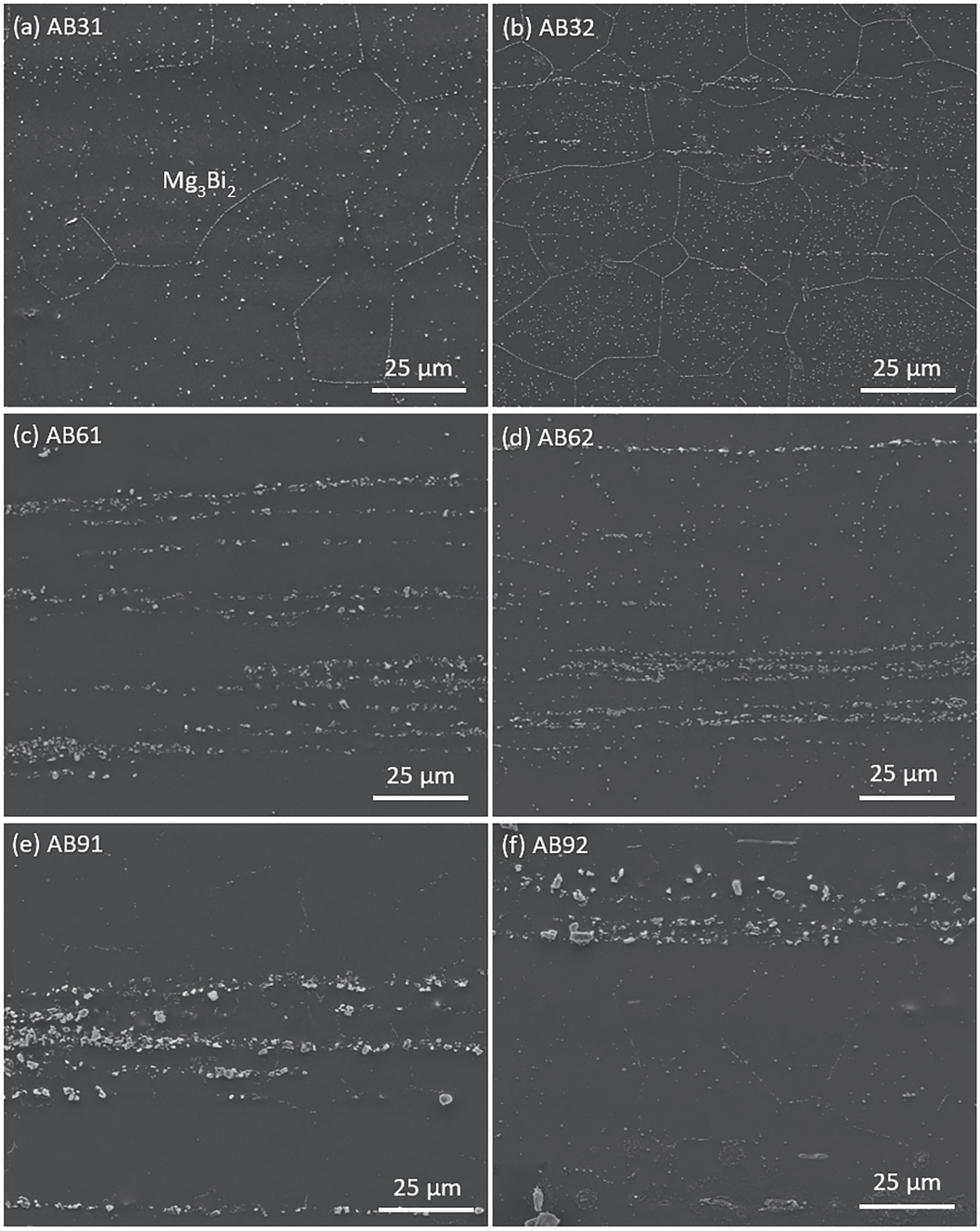

Fig. 5. Secondary electron images showing the morphology, size and distribution of the precipitates. (a) AB31: fine Mg_3Bi_2 precipitates can be seen throughout the matrix and along the grain boundaries in AB31. (b) AB32: doubling the Bi% results in more precipitates that streak in the matrix roughly along the ED. (c) AB61: increase in Al% substantial increases the streaking of precipitates across the matrix, but fewer precipitates along the grain boundaries. (d) AB62: streaking of the precipitates can also be seen. (e) AB91: The precipitates in the streaks becomes coarser. Fine precipitates along the grain boundaries can also be seen. (f) AB92: similar to AB91.

flake-like $Mg_{17}Al_{12}$ precipitates in the streaks become significantly coarser (2–3 µm) than in AB61 and AB62. Sometimes the flakes are decorated with much finer Mg_2Bi_3 precipitates. At this high Al%, plates of $Mg_{17}Al_{12}$ can be observed at the grain boundaries. Similarly, in AB92 (Fig. 6f), coarse flake-like $Mg_{17}Al_{12}$ in the matrix and $Mg_{17}Al_{12}$ plates at the grain boundaries can be observed.

The results of uniaxial tensile and compressive testing along the extrusion direction of all six Mg-Al-Bi alloys are displayed in Fig. 7. Several salient features can be observed. A tension/compression anisotropy can clearly be seen. This behavior is typical of wrought Mg alloys with a strong basal texture [5]. Yield asymmetry can also be seen with the yield stresses of tension significantly higher than that of compression. The yielding in tension is dominated by dislocation-mediated plastic deformation whereas the yielding in compression is dominated by deformation twinning [5]. In tension (Fig. 7a), the yield stress and the ultimate tensile stress consistently increase with increasing Al% and Bi%. A similar trend can be observed in compression (Fig. 7b). At the low concentration range, i.e., for AB31 and AB32, a significant increase of 34 % in yield stress and 23 % in ultimate tensile stress are observed (Fig. 7a). However, the magnitude of increase gradually decreases as both Al% and Bi% increase. Specifically, for AB61 and AB62, a 17 % increase in the yield stress and only a 7 %

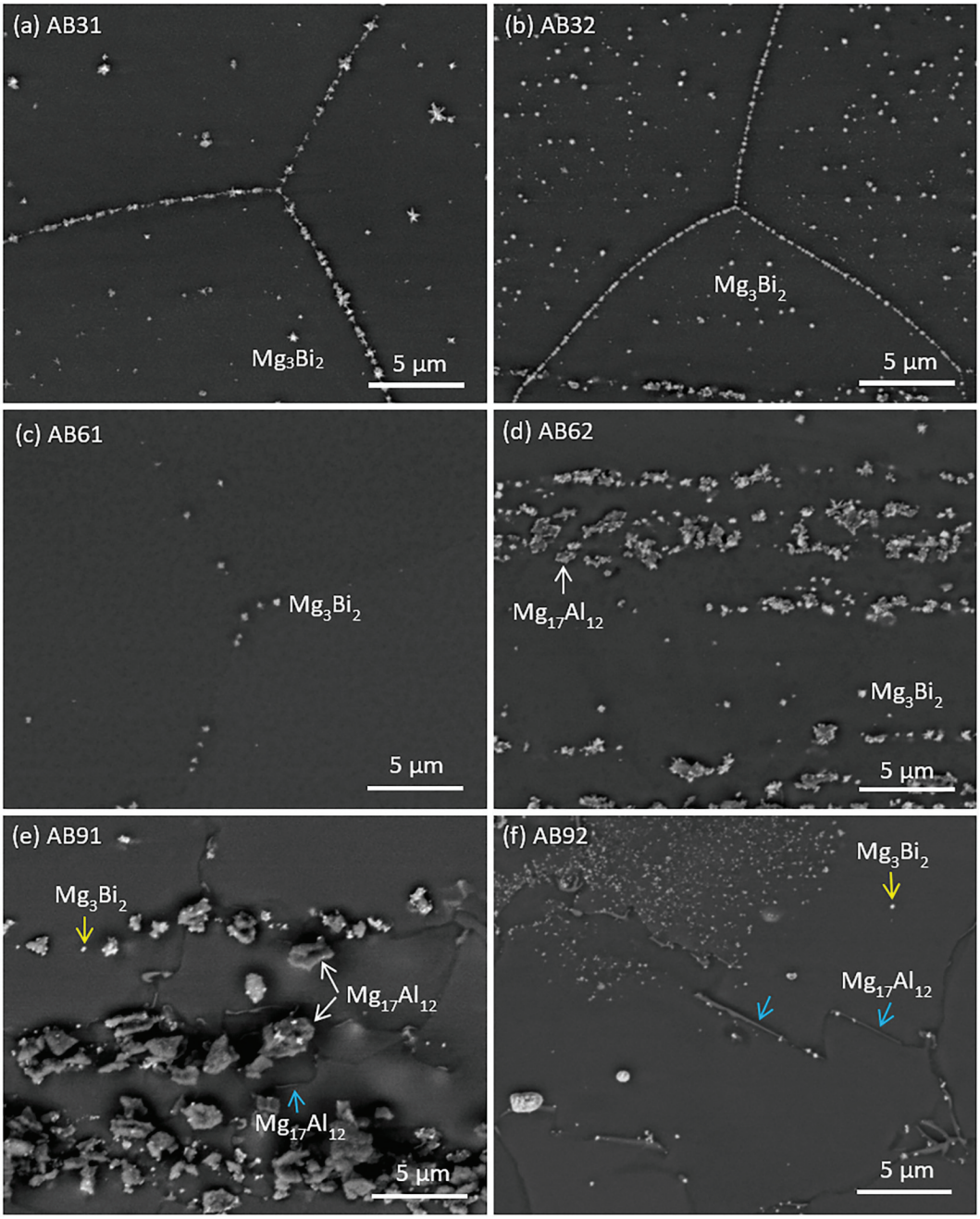

Fig. 6. Back scattered electron images of the precipitates at a higher magnification. (a) AB31: fine Mg_3Bi_2 precipitates (bright) decorate the grain boundaries and are also dispersed in the matrix. (b) AB32: more Mg_3Bi_2 precipitates as the Bi% increases. (c) AB61: fewer precipitates appear at the grain boundaries. (d) AB62: an enlarged view of the precipitates in the streaks. Flake-like $Mg_{17}Al_{12}$ precipitates are decorated with Mg_3Bi_2. (e) AB91: coarse, flake-like $Mg_{17}Al_{12}$ precipitates in the matrix decorated with Mg_2Bi_3. Note that plate-like $Mg_{17}Al_{12}$ precipitates are present at grain boundaries (indicated by the cyan arrow). (f) AB92: plate-like $Mg_{17}Al_{12}$ are present at grain boundaries (indicated by the cyan arrows). (For interpretation of the references to colour in this figure legend, the reader is referred to the Web version of this article.)

increase in the ultimate tensile stress is observed. As for AB91 and AB92, the increase in yield stress and the ultimate tensile stress further reduces down to 4 % and 3 %, respectively. These results indicate that both Al and Bi improve the strength of Mg; but in the low Al% range, increasing Bi% results in a more conspicuous strengthening effect. As the Al% increases, the strengthening effect of Bi is gradually masked out by the strengthening effect of Al. Moreover, a slight increase in the elastic modulus can be observed with increasing alloy concentration, which is likely due to the increase in volume fraction of the secondary phases. Serrations in plastic flow can also be observed for AB91 and AB92 (Fig. 7a). This may be related to the higher volume fractions of precipitates in these high concentrations and their interaction with dislocations. During tensile deformation, dislocations are initially pinned down by precipitates and then de-pinned at higher stresses, causing the observed serration. Most interestingly, despite the increase in both yield stress and ultimate tensile stress as the Al% and Bi% increase, no significant drop in ductility is observed. For instance, the ductility of AB91 and AB92 which has the highest Al% is fairly close to that of AB31 and AB32. This behavior is of particular interest to the design of new Mg alloys with improved strength while retaining reasonable ductility. As shown below, this phenomenon can be related to the unique morphology and distribution of the precipitates in these alloys.

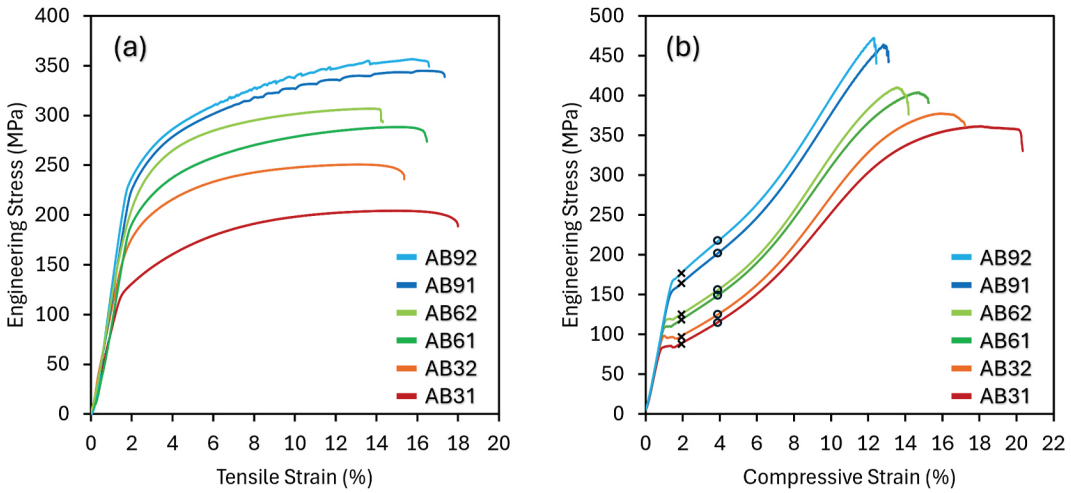

Fig. 7. (a) The tensile stress-strain curves of the six alloys. The tensile load is along the extrusion direction. As the concentration of Al and Bi increases, the yield stress and the ultimate stress increase. Interestingly, no significant drop in ductility is observed. (b) The compressive stress-strain curves of the six alloys. All the stress-strain curves present a sigmoidal shape; however, the range of low stress portion is reduced as the Al% and Bi% increase. At strain levels of 2 % and 4 % (marked by symbols of x's and o's), the compression tests were interrupted, and the specimens were prepared for EBSD scan.

In contrast to tension, the magnitude of increase in yield stress and flow stress is rather consistent in compression (Fig. 7b), i.e., increasing Bi% results in a steady increase by ~2 % in these stresses across the Al% concentration range. As the strength of the Mg-Al-Bi alloys increases, the strain to failure consistently drops, however. Yet, even the alloys with the highest Al%, i.e., AB91 and AB92, maintain significant values of strain to failure (>12 %). To analyze the effect of Al% and Bi% on the twinning behavior, interrupted compression is carried out at the strain levels of 2 % and 4 %, as indicated on the stress-strain curves.

Quantitative values of the yield stress, ultimate tensile stress and ductility in tension; the peak stress and strain to failure in compression are listed in Table 1. The yield asymmetry ratio (YAR is defined as the ratio between compression yield stress and tension yield stress) decreases continuously across AB31, AB32, AB61, and AB62, yet the YAR increases in AB91 and AB92.

Fig. 8 shows the evolution of the pole figures of the samples during compression. A center spot gradually appears at the center, indicating that the basal planes of individual grains have reoriented by nearly 90° which is typical of $\{10\bar{1}2\}$ twinning. Thus, the dominant twinning mode is $\{10\bar{1}2\}$, as expected.

4. Discussion

4.1. Effect of Al and Bi on the twinning behavior

The sigmoidal shape (Fig. 7b) of the stress-strain curves in compression along the extrusion direction suggests that deformation twinning, especially the $\{10\bar{1}2\}\langle 10\bar{1}1\rangle$ twinning mode is activated at the low stress stage plastic deformation. For AB31 and AB32, immediately after yielding, a short plateau can be observed, this could be due to the activation of basal slip that interact with the precipitates. Shortly after yielding, the density of basal dislocations is low. The basal dislocations may be hindered by the precipitates and then break away. Although the vast majority of the basal planes of individual grains are roughly parallel to the loading direction (Fig. 2), and the basal slip systems have Schmid factors close to zero, basal dislocations can still be activated because the basal slip is the easiest deformation mode in pure Mg (~1.0 MPa) and Mg alloys. One possible mechanism is that after $\{10\bar{1}2\}$ twinning, the basal planes are reoriented by a theoretical angle of 86.3° [37,38], leading to the activation of basal slip. Another possible mechanism is that, at stress concentrations such as free surfaces, grain boundaries and twin boundaries, basal slip can be activated even when the Schmid factor equals zero, which has commonly been observed in atomistic simulations [39,40]. Chen et al. [41] quantitatively measured the contribution of $\{10\bar{1}2\}$ twinning to the plastic strain in an extruded AZ31. They found that at the very early stage of plastic deformation (~0.25 % plastic strain), the contribution from $\{10\bar{1}2\}$ twins was about 14 %, indicating that the dominant deformation mode was basal dislocation slip up to that point in plastic deformation. Then the plastic deformation was quickly taken over and dominated by $\{10\bar{1}2\}$ twinning. But such a plateau did not appear in AZ31 [42]. Note that the yield stress of AB31 and AB32 in compression (Fig. 5b) is significantly lower than that of the AZ31 (~130 MPa [42]). This can be seen from the steeper slope of the low stress stage deformation. Thus, in the case of AZ31, the higher yield stress elevates the position of the yield point on the stress-strain curve and this makes less significant the difference in stress between basal slip and twinning. As the Al% is increased to 6 %, i.e., AB61 and AB62, the critical stress for basal slip goes up as a result of the strengthening effect from the higher Al%. At the higher stresses, twinning is activated quickly after the basal slip, and the range of the plateau shortens, if compared to that of AB31 and AB32. As the Al% is further increased to 9 %, i.e., AB91 and AB92, the plateau disappears.

For all the Mg-Al-Bi alloys in our work, the flow stress consistently increases as the Al% and Bi% increase, but the stress-strain curves remain nearly parallel (Fig. 7b). This indicates that both Al% and Bi% influence the twin volume fraction during plastic deformation. The range of low stress plastic deformation narrows with increasing Al% and Bi%, especially the Al%, suggesting that, as the Al% increases, the twinning activity and thus the twin volume fraction reduces. Thus, alloying with Al effectively suppresses $\{10\bar{1}2\}$ twinning at higher concentrations. To reveal this effect, we compare the twinning behavior of

Table 1
Mechanical properties of the as extruded alloys from the tension and compression stress-strain curves.

Alloy	Tension			Compression			YAR
	σ_y (MPa)	σ (MPa)	ε_f (%)	σ_y (MPa)	σ (MPa)	ε_f (%)	$\frac{\sigma_{yC}}{\sigma_{yT}}$
AB31	125	204	18.0	83	362	20.2	0.66
AB32	168	251	15.4	98	378	17.2	0.58
AB61	187	288	16.4	108	404	15.2	0.58
AB62	218	307	14.2	118	410	14.0	0.53
AB91	233	345	17.4	155	464	13.0	0.67
AB92	243	357	16.5	168	472	12.4	0.69

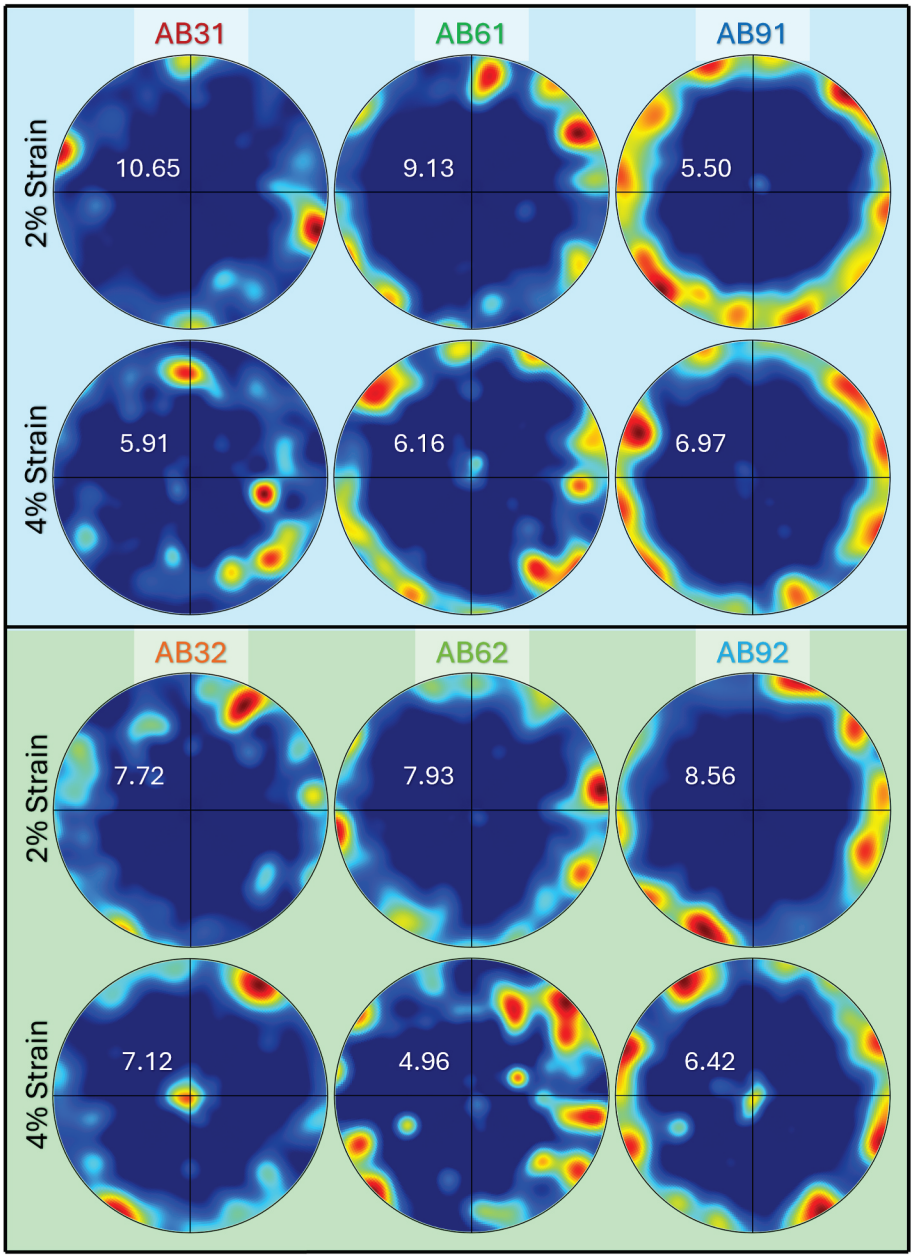

Fig. 8. The (0001) pole figures of each extruded material following 2 % or 4 % compressive strain. A center spot appears as the strain increases, indicating that the dominant twinning mode is $\{10\bar{1}2\}$.

the six Mg-Al alloys with 1.0 % Bi and results are shown in Fig. 9. In this figure, the IPF maps of samples AB31, AB61, and AB91 compressed to 2 % or 4 % are grouped and arranged for direct comparison. In Fig. 9a (AB31), when compressed to 2 % strain, lenticular $\{10\bar{1}2\}$ twins are formed but these twins are rather thin at this strain level. The majority of these extension twins are activated as a result of the reorientation of the *c*-axes of individual crystals by nearly 90° around the $\langle 11\bar{2}0\rangle$ tilt axis. Thus, the *c*-axes of the twin lattices become close to parallel to the compression direction. As the Al% is increased from 3 % to 6 % (Fig. 9b), the twinning activity apparently decreases. Further increasing the concentration of Al to 9 % (Fig. 9c) shows a significant decrease in twinning activity. As the strain increases from 2 to 4 %, AB31 has a substantial increase in twinning activity as more extension twins are nucleated and grow, and the twins thicken or coalesce with increasing strain (Fig. 9d). After 4 % strain, AB61 (Fig. 9e) presents a similar trend with more twin nucleation and thickening. In contrast, at the highest Al%, AB91 shows a much-reduced twin number density and area fraction, compared to AB31 and AB61, which is consistent with the stress-strain curves (Fig. 7). From these IPF maps, we can obtain twin volume fraction by measuring the twin area fraction (these two quantities have the same statistical significance). The twin area fractions are computed as $\frac{A_{twin}}{A_{total}}$, where the twinned area A_{twin} (in number of pixels) is measured from these IPF maps by extracting the twinned areas from the parent grains. The results are shown in Fig. 9g and h. It can be seen that the twin area fraction consistently decreases with increasing Al%, especially at 9 % Al.

Fig. 10 compares the effect of Al% on twinning in the 2 % Bi containing alloys, i.e., AB32, AB62, and AB92. At 2 % strain, fine extension twins can be observed in AB32, in contrast, very few extension twins are observed in AB62 and AB92, maintaining the trend from Fig. 10a–c. This implies that alloying with Al in this Mg-Al-Bi ternary system effectively suppresses $\{10\bar{1}2\}$ twinning. At 4 % strain, the extension twins in AB32 (Fig. 10b) appear to be coarser than at 2 % (Fig. 10a). By comparison at

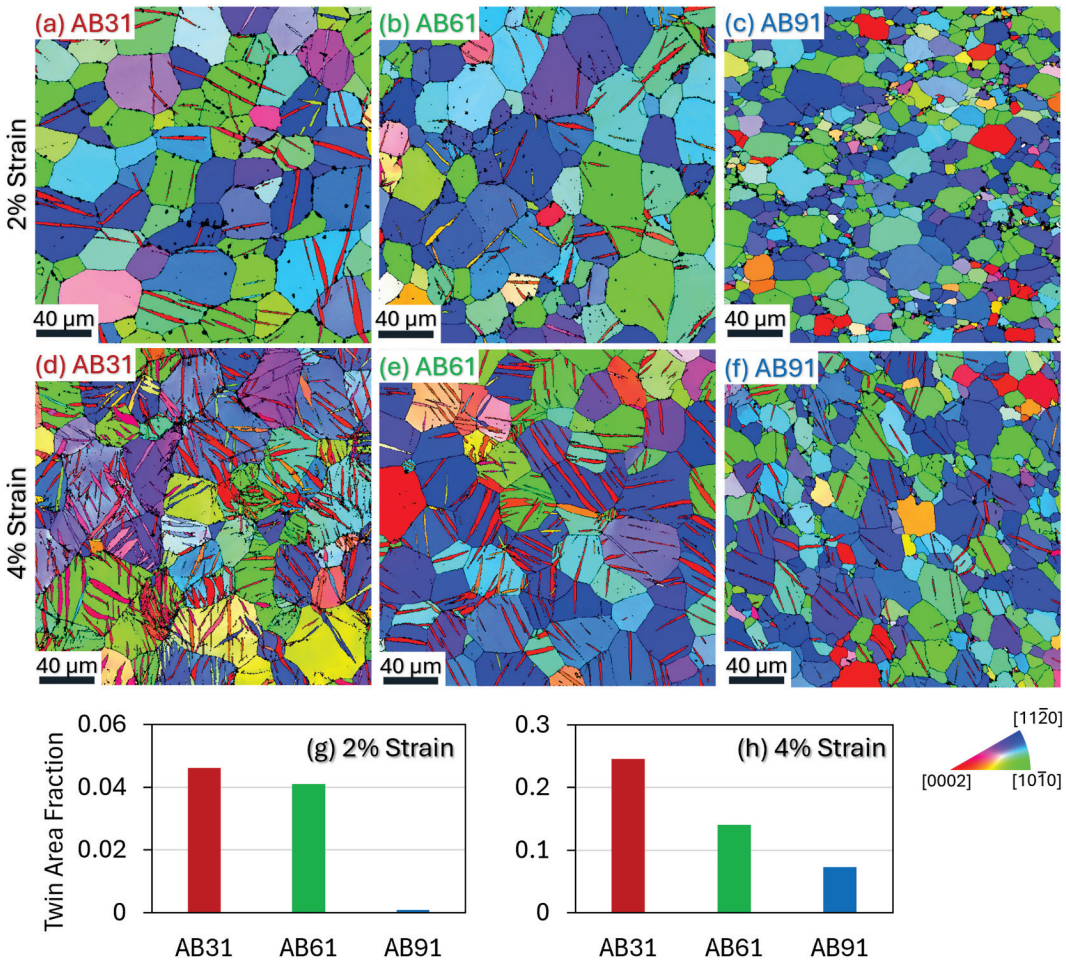

Fig. 9. Twinning behavior of the as extruded 1 % Bi samples after interrupted compression. (a) AB31 at 2 % strain. Thin twins can be seen. (b) AB61 at 2 % strain. Fine twins can be seen. (c) AB91 at 2 % strain. Very few twins are present. (d) AB31 at 4 % strain. Twin density increases and twins coarsen rapidly. (e) AB61 at 4 % strain. Twin density increases. (f) AB91 at 4 % strain. Twin density is low and the twins are very fine. The EBSD scans are conducted on the cross-sections perpendicular to the extrusion direction. Overall, twinning activity drops with increasing Al%.

4 % strain, AB62 and AB92 (Fig. 10e and f) have fewer and finer extension twins than AB32 (Fig. 10d). The quantitative measurements of the twin area fraction of AB32, AB62 and AB92 at strains of 2 % and 4 % are shown in Fig. 10g and h. Again, the results show that $\{10\bar{1}2\}$ twinning is significantly reduced with increasing Al%.

The IPF maps and the measurements of twin area fraction (Figs. 9 and 10) show that alloying with Al suppresses $\{10\bar{1}2\}$ twinning. This effect of Al on $\{10\bar{1}2\}$ twinning is consistent with the literature reports. Guo et al. [43] studied the effect of Al on the deformation behavior during hot rolling of Mg-Al-Zn alloys in which 3 %, 6 % and 9 % Al were added to the alloys. Their results showed that the extension twinning was strongly suppressed as Al% was increased. Bian et al. [44] observed similar effect of Al on the twinning behavior of Mg-Al-Mn alloys with Al % in the range of 1 %–4 %. They showed that the relative $\{10\bar{1}2\}$ twinning activity decreased with increasing Al content. However, the yield strengths of both tension and compression decreased with increasing Al%, opposite to the trend in our Mg-Al-Bi alloys. In an experimental study of twinning-detwinning during cyclic loading of alloyed and unalloyed Mg using high energy X-ray diffraction, Murphy-Leonard et al. [45] showed that Al increased the stress for $\{10\bar{1}2\}$ twin growth. As a result, it would be harder for $\{10\bar{1}2\}$ twins to grow with increasing Al%. Atomistic simulations also showed a similar effect of Al on $\{10\bar{1}2\}$ twinning. Wang [46] investigated the effect of Al on extension twinning in Mg using molecular dynamics simulations and density functional theory calculations. It was shown that the twin volume fraction constantly decreased as more Al atoms were added into the atomistic simulation system.

The stress-strain curves of compression tests (Fig. 7b) indicate that the addition of Bi also has an effect on the twinning behavior as the Bi% increases from 1 % to 2 %. We can see this effect by comparing the twin area fraction at 4 % strain between AB31 (Fig. 9d) and AB32 (Fig. 10d), AB61(Fig. 9e) and AB62 (Fig. 10e), AB91 (Fig. 9f) and AB92 (Fig. 10f). At lower Al% concentrations, i.e., 3 % and 6 %, the effect of Bi% on $\{10\bar{1}2\}$ twinning is not as conspicuous as Al% (Fig. 9g and h and Fig. 10g and h). But at high Al%, i.e., AB92, the twin area fraction is slightly less than that of AB91.

The effect of Bi on the twinning behavior of Mg alloys is much less studied and not well understood. Bi has a pretty large solubility (~9 %) in Mg near the eutectic temperature (553 °C). At room temperature, most of the Bi goes to the Mg_3Bi_2 intermetallic phase after solidification. After extrusion, the Mg_3Bi_2 precipitates remain in the matrix of α-Mg. On the one hand, these Mg_3Bi_2 precipitates, along with the β-$Mg_{17}Al_{12}$, strengthen the α-Mg matrix and thus increase the critical stresses for dislocation slip. In terms of $\{10\bar{1}2\}$ twin nucleation, the activation volume for twin nucleation could be larger than dislocation nucleation because highly coordinated atomic shuffles are required for this twinning mode [9,47,48]. These atomic shuffles transform the basal plane of the matrix lattice into the prismatic plane of the twin lattice as this pair of planes are corresponding planes [47,48]. Thus, after twinning, the *c*-axis of parent lattice is reorientated by nearly 90° [47,48]. Hence,

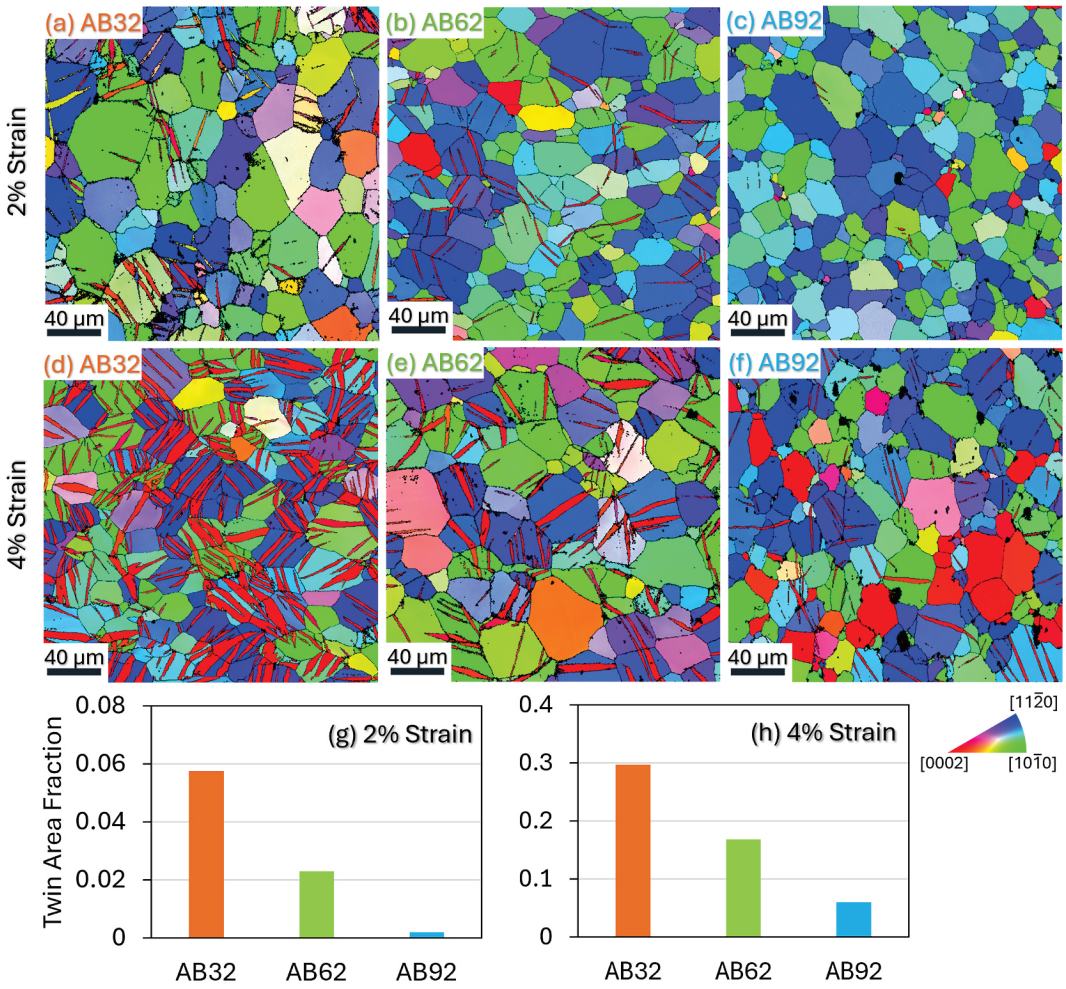

Fig. 10. Twinning behavior of the as extruded 2 % Bi samples after interrupted compression. (a) AB32 at 2 % strain. Twins are activated. (b) AB62 at 2 % strain. Thin twins are activated. (c) AB92 at 2 % strain. Very few twins can be seen. (d) AB32 at 4 % strain. More twins are formed and the twins coarsen. (e) AB62 at 4 % strain. The EBSD scans are conducted on the cross-sections perpendicular to the extrusion direction. Similar to the trend in Fig. 9, the amount of twinning significantly decreases with increasing Al% along with the higher Bi%.

pre-existing dislocations in the matrix promote twin nucleation because the elastic strains near the dislocation core help accommodate the misfit strain at the twin boundaries which are usually highly incoherent [49]. During $\{10\bar{1}2\}$ twinning, a misfit strain is produced along the *c*-axis, which equals $\frac{\sqrt{3}-\gamma}{\gamma} \approx 6.7$ % (γ is the *c*/*a* ratio, 1.624 for Mg), whereas a contraction is produced along the $\langle 10\bar{1}0\rangle$ direction [48]. This misfit strain along the [0002] effectively accommodates the tensile deformation along the *c*-axis. This strain accommodation is fundamentally different from that of twinning dislocations that must glide on the theoretical twinning plane. When the Al% and Bi% increase, the critical stresses for dislocation nucleation and slip increase, and this reduces the probability of twin nucleation. Moreover, numerous experimental observations and atomistic simulations indicate that $\{10\bar{1}2\}$ is not mediated by twinning dislocations [47–51], contrary to the classical twinning theory. Gharghouri et al. [52] observed that precipitates in Mg alloys could be completely engulfed by the $\{10\bar{1}2\}$ twins without leaving any trace of plastic shearing. They also found that the $\{10\bar{1}2\}$ twins did not have constant habit planes or twin boundaries and they could easily bypass the precipitates. Using *in-situ* TEM, Liu et al. [53] observed similar twin-precipitate interaction in Mg alloys, in which $\{10\bar{1}2\}$ twin boundaries migrated around the precipitates and bypassed them. These experimental observations, along with many others [51,54,55], confirm that there should not be any twinning dislocations at $\{10\bar{1}2\}$ twin boundaries. Thus, the effect of precipitates on $\{10\bar{1}2\}$ twinning is expected to be limited and dependent on the strength of the interface between the precipitate and the Mg matrix, as well as the volume fraction of the precipitates. As the Bi% increases, the volume fraction of Mg_3Bi_2 increases, and the stress for twin growth increases accordingly. This effect is reflected in the slight shift of the stress-strain curves in compression along the extrusion direction (Fig. 7b).

4.2. *Effect of Bi on the ductility of Mg-Al alloys*

Perhaps the most interesting feature in the stress-strain curves is the insignificant reduction in tensile ductility (Fig. 7a) across the whole range of Al concentration from 3 % to 9 %. Despite the significant improvement in strength at the high Al concentrations, the ductility is still maintained. Although the strain to failure in compression decreases, the strains for AB91 and AB92 alloys remain greater than 12 % which are higher than wrought AZ91 (Fig. 7b). The reduced strain to failure in compression can be related to twinning that is activated and dominates the low stress stage deformation. After twinning, the matrix is reoriented by ~90°, which changes the orientation relationship between the matrix and the precipitates. This change may also weaken the interfacial bonding between the precipitates and the matrix, resulting in reduced strain to failure [56]. These results indicate that a small addition of Bi (<1.0 %) to Mg-Al alloys would be beneficial for ductility. This is particularly important for design of new Mg alloys with good ductility

while retaining high strength.

There have been reports that adding Bi to Mg alloys positively affects their mechanical properties. Recently, Shen et al. [57] conducted high-throughput DFT calculations of how alloying elements affected the generalized stacking fault energy on $\{10\bar{1}1\}$ pyramidal-I and $\{11\bar{2}2\}$ pyramidal-II slip planes. Specifically, the unstable stacking fault energy is a measure of the energy barrier to dislocation nucleation and glide, and a lower value (in reference to pure Mg) is preferred for better ductility. These pyramidal dislocations are the only slip systems that can accommodate the strains along the *c*-axis because the Burgers vectors $\frac{1}{3}\langle 11\bar{2}3\rangle$ have a component along the *c*-axis. Their calculations screened a total of 54 elements in the Periodic Table. The formation enthalpy of solid solutions was also calculated. Their results showed that Bi is one of the promising candidates that could reduce the unstable stacking fault energy on the two pyramidal slip planes. Thus, Bi is expected to promote pyramidal dislocation slip in Mg alloys. It has been shown that the low ductility of Mg and Mg alloys is partly due to the lack of sufficient active pyramidal slip systems that have a critical stress about one to two orders of magnitude higher than basal slip [58]. Thus, activating more pyramidal slip systems would greatly benefit the ductility. Meng et al. [26] developed a rare-earth free Mg-1.32Bi-0.72Ca alloy. A single step extrusion was conducted on the cast ingot after homogenization and the extrusion temperature was 300 °C. They found that the basal texture was weakened after extrusion and the extruded samples presented a very high tensile ductility (~43 %). This extraordinary ductility was attributed to the refined grain size (~6.3 μm) and the weakened basal texture. Their TEM work showed that non-basal pyramidal dislocation slip became the main deformation mode that gave rise to the high ductility. Somekawa and Singh [59] studied the mechanical properties of dilute Mg-Bi alloys after extrusion. A fine grain size (~1.2 μm) was obtained in the extruded samples. Superior ductility (170 %) at room temperature was observed when Bi% was 0.3 at%, but the ductility decreased with increasing Bi%. The superior ductility was attributed to grain boundary sliding in the fine-grained microstructure. The effect of Bi on as-cast AZ31, AZ61 and AZ91 alloys was studied by Moshaver et al. [60]. They reported that optimal strength and ductility were achieved when the Bi% was about 1.0 %. But the workability and formability decreased with greater Bi concentration. The relatively better ductility of the AB alloys than AZ alloys is also related to the morphology, size and distribution of the precipitates. From Figs. 5 and 6, alloying with Bi suppresses the formation of $Mg_{17}Al_{12}$ precipitates that are plate-like along the basal planes in Mg-Al alloys [36]. The fine, spherical Mg_3Bi_2 precipitates are more beneficial for ductility than plate-like $Mg_{17}Al_{12}$. The literature reports and the results in our work (Fig. 7) suggest that Bi is indeed beneficial for the ductility of Mg alloys, but the concentration should be at the low end or less than 1.0 %.

5. Conclusions

In this work, we systematically investigate the effects of Al and Bi on the deformation behavior of extruded Mg-Al-Bi alloys with the Al% of 3~9 wt% and Bi% of 1~2 wt%. The following conclusions can be drawn.

1. Addition of Bi suppresses the formation of plate-like β-$Mg_{17}Al_{12}$ precipitates that are commonly observed in the AZ Mg alloys. For low alloy compositions (Al = 3 % and Bi = 1–2 %), fine (hundreds of nanometers) precipitates are formed in the matrix and at the grain boundaries. As the alloy concentration increases, the precipitates become coarser, and form streaks along the extrusion direction across the grains.
2. The strength of the AB alloys increases with increasing Al% and Bi%. However, interestingly, the tensile ductility is not significantly affected by the increasing alloy concentration, and a fairly good ductility (14 %–18 %) is retained across the range of concentrations. The strain to failure in compression decreases but retains greater than 12 %. This behavior can be related to the refined precipitates by the addition of Bi.
3. The activity of $\{10\bar{1}2\}$ extension twinning consistently decreases with increasing Al% and Bi%, indicating that in the Mg-Al-Bi alloys, $\{10\bar{1}2\}$ twinning is suppressed as the Al% and Bi% increases. Alloying with Al effectively suppresses $\{10\bar{1}2\}$ twinning, especially at high concentrations. This effect may be beneficial to mitigate the yield asymmetry and tension/compression anisotropy that is widely observed in wrought Mg alloys.
4. Based on our results, an optimal Bi% less than 1.0 % is suggested for high strength Mg-Al-Bi alloys while much of the ductility is still retained.

CRediT authorship contribution statement

A. Goldman: Writing – original draft, Methodology, Investigation, Formal analysis, Data curation. **Z.G. Xu:** Writing – review & editing, Formal analysis, Data curation. **B. Li:** Writing – review & editing, Supervision, Resources, Project administration, Methodology, Investigation, Funding acquisition, Formal analysis, Conceptualization. **Y.L. Liao:** Writing – review & editing, Resources, Formal analysis. **A. Jordan:** Resources, Methodology, Data curation.

Declaration of competing interest

The authors declare that they have no known competing financial interests or personal relationships that could have appeared to influence the work reported in this paper.

Acknowledgements

BL thanks the support from the US National Science Foundation (CMMI-2032483).

Data availability

Data will be made available on request.

References

[1] T. Abbott, Heat treating of magnesium alloys. https://doi.org/10.31399/asm.hb.v04e.a0006254, 2016.
[2] L. Čížek, M. Greger, L. Pawlica, L.A. Dobrzański, T. Tański, Study of selected properties of magnesium alloy AZ91 after heat treatment and forming, J. Mater. Process. Technol. 157–158 (2004) 466–471, https://doi.org/10.1016/j.jmatprotec.2004.07.149.
[3] J.-F. Nie, Precipitation and hardening in magnesium alloys, Metall. Mater. Trans. A 43 (2012) 3891–3939, https://doi.org/10.1007/s11661-012-1217-2.
[4] S.R. Agnew, Wrought magnesium: a 21st century outlook, JOM 56 (2004) 20–21, https://doi.org/10.1007/s11837-004-0120-8.
[5] J.F. Nie, K.S. Shin, Z.R. Zeng, Microstructure, deformation, and property of wrought magnesium alloys, Metall. Mater. Trans. A 51 (2020) 6045–6109, https://doi.org/10.1007/s11661-020-05974-z.
[6] J. Wu, L. Jin, J. Dong, F. Wang, S. Dong, The texture and its optimization in magnesium alloy, J. Mater. Sci. Technol. 42 (2020) 175–189, https://doi.org/10.1016/j.jmst.2019.10.010.
[7] S.R. Agnew, Ö. Duygulu, Plastic anisotropy and the role of non-basal slip in magnesium alloy AZ31B, Int. J. Plast. 21 (2005) 1161–1193, https://doi.org/10.1016/j.ijplas.2004.05.018.
[8] E.A. Ball, P.B. Prangnell, Tensile-compressive yield asymmetries in high strength wrought magnesium alloys, Scripta Metall. Mater. 31 (1994) 111–116, https://doi.org/10.1016/0956-716X(94)90159-7.
[9] Y. Chino, K. Kimura, M. Hakamada, M. Mabuchi, Mechanical anisotropy due to twinning in an extruded AZ31 Mg alloy, Mater. Sci. Eng. A 485 (2008) 311–317, https://doi.org/10.1016/j.msea.2007.07.076.
[10] R.B. Figueiredo, M.T.P. Aguilar, P.R. Cetlin, T.G. Langdon, Processing magnesium alloys by severe plastic deformation, IOP Conf. Ser. Mater. Sci. Eng. 63 (2014) 012171, https://doi.org/10.1088/1757-899X/63/1/012171.
[11] D. Griffiths, Explaining texture weakening and improved formability in magnesium rare Earth alloys, Mater. Sci. Technol. 31 (2015) 10–24, https://doi.org/10.1179/1743284714Y.0000000632.
[12] J. Koike, T. Kobayashi, T. Mukai, H. Watanabe, M. Suzuki, K. Maruyama, K. Higashi, The activity of non-basal slip systems and dynamic recovery at room

temperature in fine-grained AZ31B magnesium alloys, Acta Mater. 51 (2003) 2055–2065, https://doi.org/10.1016/S1359-6454(03)00005-3.
[13] A.A. Luo, Recent magnesium alloy development for elevated temperature applications, Int. Mater. Rev. 49 (2004) 13–30, https://doi.org/10.1179/095066004225010497.
[14] J. Wu, L. Jin, J. Dong, F. Wang, S. Dong, The texture and its optimization in magnesium alloy, J. Mater. Sci. Technol. 42 (2020) 175–189, https://doi.org/10.1016/j.jmst.2019.10.010.
[15] G.I. Taylor, Plastic strain in metals, Plast. Strain Met. (1938) 307–324.
[16] X. Guo, S. Remennik, C. Xu, D. Shechtman, Development of Mg–6.0%Zn–1.0% Y–0.6%Ce–0.6%Zr magnesium alloy and its microstructural evolution during processing, Mater. Sci. Eng. A 473 (2008) 266–273, https://doi.org/10.1016/j.msea.2007.03.083.
[17] S.-J. Meng, H. Yu, S.-D. Fan, Q.-Z. Li, S.H. Park, J.S. Suh, Y.M. Kim, X.-L. Nan, M.-Z. Bian, F.-X. Yin, W.-M. Zhao, B.S. You, K.S. Shin, Recent progress and development in extrusion of rare Earth free Mg alloys: a review, Acta Metall. Sin. Engl. Lett. 32 (2019) 145–168, https://doi.org/10.1007/s40195-018-00871-2.
[18] J. Xing, X. Yang, H. Miura, T. Sakai, Mechanical properties of magnesium alloy AZ31 after severe plastic deformation, Mater. Trans. 49 (2008) 69–75, https://doi.org/10.2320/matertrans.ME200705.
[19] B. Xu, J. Sun, Z. Yang, L. Xiao, H. Zhou, J. Han, H. Liu, Y. Wu, Y. Yuan, X. Zhuo, D. Song, J. Jiang, A. Ma, Microstructure and anisotropic mechanical behavior of the high-strength and ductility AZ91 Mg alloy processed by hot extrusion and multi-pass RD-ECAP, Mater. Sci. Eng. A 780 (2020) 139191, https://doi.org/10.1016/j.msea.2020.139191.
[20] A. Yamashita, Z. Horita, T.G. Langdon, Improving the mechanical properties of magnesium and a magnesium alloy through severe plastic deformation, Mater. Sci. Eng. A 300 (2001) 142–147, https://doi.org/10.1016/S0921-5093(00)01660-9.
[21] W. Yuan, R.S. Mishra, B. Carlson, R.K. Mishra, R. Verma, R. Kubic, Effect of texture on the mechanical behavior of ultrafine grained magnesium alloy, Scr. Mater. 64 (2011) 580–583, https://doi.org/10.1016/j.scriptamat.2010.11.052.
[22] H. Ding, X. Shi, Y. Wang, G. Cheng, S. Kamado, Texture weakening and ductility variation of Mg–2Zn alloy with CA or RE addition, Mater. Sci. Eng. A 645 (2015) 196–204, https://doi.org/10.1016/j.msea.2015.08.025.
[23] D.G.J. Griffiths, Understanding Texture Weakening in Magnesium Rare Earth Alloys, Ph.D., The University of Manchester, United Kingdom, 2015. https://www.proquest.com/docview/1775231789/abstract/DF3D7F6A3ABB415DPQ/1. (Accessed 10 January 2025).
[24] J.W. Cha, S.-C. Jin, J.-G. Jung, S.H. Park, Effects of homogenization temperature on microstructure and mechanical properties of high-speed-extruded Mg–5Bi–3Al alloy, J. Magnesium Alloys 10 (2022) 2833–2846, https://doi.org/10.1016/j.jma.2021.07.007.
[25] J. Go, S.-C. Jin, H. Kim, H. Yu, S.H. Park, Novel Mg–Bi–Al alloy with extraordinary extrudability and high strength, J. Alloys Compd. 843 (2020) 156026, https://doi.org/10.1016/j.jallcom.2020.156026.
[26] S.J. Meng, H. Yu, S.D. Fan, Y.M. Kim, S.H. Park, W.M. Zhao, B.S. You, K.S. Shin, A high-ductility extruded Mg-Bi-Ca alloy, Mater. Lett. 261 (2020) 127066, https://doi.org/10.1016/j.matlet.2019.127066.
[27] Y. Guangyin, S. Yangshan, D. Wenjiang, Effects of bismuth and antimony additions on the microstructure and mechanical properties of AZ91 magnesium alloy, Mater. Sci. Eng. A 308 (2001) 38–44, https://doi.org/10.1016/S0921-5093(00)02043-8.
[28] Z. Xu, H. Zhang, P. Krishnan, C. Hale, L.J. Kecskes, S. Yarmolenko, S. Fialkova, Q. Wei, J. Sankar, Non-conventional hot rolling for improvement of mechanical properties in binary Mg-alloys, Mech. Mater. 164 (2022) 104111, https://doi.org/10.1016/j.mechmat.2021.104111.
[29] B. Beausir, J.J. Fundenberger, Analysis Tools for Electron and X-ray Diffraction, ATEX-Softw. Www Atex-Softw. Eu Univ. Lorraine-Metz, 2017, p. 201. https://scholar.google.com/scholar?cluster=9903197906207928456&hl=en&oi=scholarr. (Accessed 23 December 2024).
[30] A.G. Beer, M.R. Barnett, Microstructural development during hot working of Mg-3Al-1Zn, Metall. Mater. Trans. A 38 (2007) 1856–1867, https://doi.org/10.1007/s11661-007-9207-5.
[31] J.D. Robson, D.T. Henry, B. Davis, Particle effects on recrystallization in magnesium–manganese alloys: particle-stimulated nucleation, Acta Mater. 57 (2009) 2739–2747, https://doi.org/10.1016/j.actamat.2009.02.032.
[32] T.T. Sasaki, T. Ohkubo, K. Hono, Precipitation hardenable Mg–Bi–Zn alloys with prismatic plate precipitates, Scr. Mater. 61 (2009) 72–75, https://doi.org/10.1016/j.scriptamat.2009.03.015.
[33] Q. Wang, H. Zhai, L. Wang, J. Xu, Y. Chen, B. Jiang, A new strong and ductile multicomponent rare-earth free Mg–bi-Based alloy achieved by extrusion and subsequent short-term annealing, Mater. Sci. Eng. A 860 (2022) 144309, https://doi.org/10.1016/j.msea.2022.144309.
[34] A.A. Nayeb-Hashemi, J.B. Clark, Phase Diagrams of Binary Magnesium Alloys, ASM International, Metals Park, Ohio, 1988.
[35] T. Guo, X. Lu, R.K. Varma, C. Zhao, J. Wang, J. You, J. Chen, Influence of coarse Mg3Bi2 particles on deformation behaviors of Mg-Bi alloys, Front. Mater. 8 (2021). https://www.frontiersin.org/articles/10.3389/fmats.2021.633789. (Accessed 9 February 2023).
[36] J.B. Clark, Age hardening in a Mg-9 wt.% Al alloy, Acta Metall. 16 (1968) 141–152, https://doi.org/10.1016/0001-6160(68)90109-0.
[37] M.R. Barnett, Twinning and the ductility of magnesium alloys: part I: "Tension" twins, Mater. Sci. Eng. A 464 (2007) 1–7, https://doi.org/10.1016/j.msea.2006.12.037.
[38] J.W. Christian, S. Mahajan, Deformation twinning, Prog. Mater. Sci. 39 (1995) 1–157, https://doi.org/10.1016/0079-6425(94)00007-7.
[39] F.X. Wang, B. Li, Origin of deflection of precipitates during interaction with a migrating twin boundary in magnesium alloys, Comput. Mater. Sci. 154 (2018) 472–480, https://doi.org/10.1016/j.commatsci.2018.08.020.
[40] Y. He, Z. Fang, B. Li, C. Wang, S.X. Mao, *In-situ* HRTEM observations of intermediate phase transformation in lattice reorientation in HCP rhenium, J. Mater. Sci. Technol. 206 (2025) 15–25, https://doi.org/10.1016/j.jmst.2024.04.023.
[41] P. Chen, B. Li, D. Culbertson, Y. Jiang, Twin-slip interaction at low stress stage deformation in an AZ31 Mg alloy, in: D. Orlov, V. Joshi, K.N. Solanki, N. R. Neelameggham (Eds.), Magnes. Technol. 2018, Springer International Publishing, Cham, 2018, pp. 193–198, https://doi.org/10.1007/978-3-319-72332-7_30.
[42] S. Mueller, K. Mueller, H. Tao, W. Reimers, Microstructure and mechanical properties of the extruded Mg-alloys AZ31, AZ61, AZ80, Int. J. Mater. Res. 97 (2006) 1384–1391, https://doi.org/10.3139/146.101382.
[43] F. Guo, D. Zhang, H. Wu, L. Jiang, F. Pan, The role of Al content on deformation behavior and related texture evolution during hot rolling of Mg-Al-Zn alloys, J. Alloys Compd. 695 (2017) 396–403, https://doi.org/10.1016/j.jallcom.2016.10.222.
[44] M.Z. Bian, A. Tripathi, H. Yu, N.D. Nam, L.M. Yan, Effect of aluminum content on the texture and mechanical behavior of Mg–1 wt% Mn wrought magnesium alloys, Mater. Sci. Eng. A 639 (2015) 320–326, https://doi.org/10.1016/j.msea.2015.05.022.
[45] A.D. Murphy-Leonard, D.C. Pagan, A. Beaudoin, M.P. Miller, J.E. Allison, Quantification of cyclic twinning-detwinning behavior during low-cycle fatigue of pure magnesium using high energy X-ray diffraction, Int. J. Fatig. 125 (2019) 314–323, https://doi.org/10.1016/j.ijfatigue.2019.04.011.
[46] F. Wang, Energetics Calculation of {10-12} Twin Nucleation and Growth in Magnesium and Alloys using Density Functional Theory and Atomistic Simulation. http://hdl.handle.net/11714/6721, 2019. (Accessed 10 January 2025).
[47] B. Li, E. Ma, Atomic shuffling dominated mechanism for deformation twinning in magnesium, Phys. Rev. Lett. 103 (2009) 035503, https://doi.org/10.1103/PhysRevLett.103.035503.
[48] B. Li, X.Y. Zhang, Twinning with zero twinning shear, Scr. Mater. 125 (2016) 73–79, https://doi.org/10.1016/j.scriptamat.2016.07.004.
[49] X.Y. Zhang, B. Li, X.L. Wu, Y.T. Zhu, Q. Ma, Q. Liu, P.T. Wang, M.F. Horstemeyer, Twin boundaries showing very large deviations from the twinning plane, Scr. Mater. 67 (2012) 862–865, https://doi.org/10.1016/j.scriptamat.2012.08.012.
[50] J. Tu, S. Zhang, On the 10 1 2 twinning growth mechanism in hexagonal close-packed metals, Mater. Des. 96 (2016) 143–149, https://doi.org/10.1016/j.matdes.2016.02.002.
[51] J. Wang, S.K. Yadav, J.P. Hirth, C.N. Tomé, I.J. Beyerlein, Pure-shuffle nucleation of deformation twins in hexagonal-close-packed metals, Mater. Res. Lett. 1 (2013) 126–132, https://doi.org/10.1080/21663831.2013.792019.
[52] M.A. Gharghouri, G.C. Weatherly, J.D. Embury, The interaction of twins and precipitates in a Mg-7.7 at.% Al alloy, Philos. Mag. A 78 (1998) 1137–1149, https://doi.org/10.1080/01418619808239980.
[53] B.-Y. Liu, N. Yang, J. Wang, M. Barnett, Y.-C. Xin, D. Wu, R.-L. Xin, B. Li, R. L. Narayan, J.-F. Nie, J. Li, E. Ma, Z.-W. Shan, Insight from *in situ* microscopy into which precipitate morphology can enable high strength in magnesium alloys, J. Mater. Sci. Technol. 34 (2018) 1061–1066, https://doi.org/10.1016/j.jmst.2018.01.017.
[54] Y. He, B. Li, C. Wang, S.X. Mao, Direct observation of dual-step twinning nucleation in hexagonal close-packed crystals, Nat. Commun. 11 (2020) 2483, https://doi.org/10.1038/s41467-020-16351-0.
[55] X.Y. Zhang, B. Li, X.L. Wu, Y.T. Zhu, Q. Ma, Q. Liu, P.T. Wang, M.F. Horstemeyer, Twin boundaries showing very large deviations from the twinning plane, Scr. Mater. 67 (2012) 862–865, https://doi.org/10.1016/j.scriptamat.2012.08.012.
[56] F.X. Wang, B. Li, Atomistic calculations of surface and interfacial energies of Mg17Al12–Mg system, J. Magnesium Alloys 6 (2018) 375–383, https://doi.org/10.1016/j.jma.2018.08.005.
[57] Y. Shen, H. Wang, B. Li, Q. An, First principles high-throughput screening to enhance the ductility of lightweight magnesium alloys, Phys. Rev. Mater. 3 (2019) 053603, https://doi.org/10.1103/PhysRevMaterials.3.053603.
[58] W.B. Hutchinson, M.R. Barnett, Effective values of critical resolved shear stress for slip in polycrystalline magnesium and other hcp metals, Scr. Mater. 63 (2010) 737–740, https://doi.org/10.1016/j.scriptamat.2010.05.047.
[59] H. Somekawa, A. Singh, Superior room temperature ductility of magnesium dilute binary alloy via grain boundary sliding, Scr. Mater. 150 (2018) 26–30, https://doi.org/10.1016/j.scriptamat.2018.02.034.
[60] H. Moshaver, M. Haddad Sabzevar, M. Mazinani, M. Mahmoudi, Effect of bismuth on microstructure, mechanical properties and fracture behavior of AZ magnesium alloys, Mater. Sci. Eng. A 854 (2022) 143676, https://doi.org/10.1016/j.msea.2022.143676.